nature materials

ARTICLES

PUBLISHED ONLINE: 26 APRIL 2009 | DOI: 10.1038/NMAT2432

Electric modulation of conduction in multiferroic Ca-doped $BiFeO_3$ films

C.-H. Yang[1]*, J. Seidel[1,2], S. Y. Kim[3], P. B. Rossen[3], P. Yu[1], M. Gajek[1], Y. H. Chu[4], L. W. Martin[2,3], M. B. Holcomb[1,2], Q. He[1], P. Maksymovych[5], N. Balke[3,5], S. V. Kalinin[5], A. P. Baddorf[5], S. R. Basu[3], M. L. Scullin[3] and R. Ramesh[1,2,3]

Many interesting materials phenomena such as the emergence of high-T_c superconductivity in the cuprates and colossal magnetoresistance in the manganites arise out of a doping-driven competition between energetically similar ground states. Doped multiferroics present a tantalizing evolution of this generic concept of phase competition. Here, we present the observation of an electronic conductor–insulator transition by control of band-filling in the model antiferromagnetic ferroelectric $BiFeO_3$ through Ca doping. Application of electric field enables us to control and manipulate this electronic transition to the extent that a p–n junction can be created, erased and inverted in this material. A 'dome-like' feature in the doping dependence of the ferroelectric transition is observed around a Ca concentration of ∼1/8, where a new pseudo-tetragonal phase appears and the electric modulation of conduction is optimized. Possible mechanisms for the observed effects are discussed on the basis of the interplay of ionic and electronic conduction. This observation opens the door to merging magnetoelectrics and magnetoelectronics at room temperature by combining electronic conduction with electric and magnetic degrees of freedom already present in the multiferroic $BiFeO_3$.

Insulator–conductor transitions have been studied theoretically and experimentally in a variety of systems[1–5]. Typical control parameters for these transitions are chemical doping, magnetic field, pressure, temperature and thickness. From an applications perspective, electric field is an especially useful control parameter, as electrodes are easily embedded in integrated devices through capacitor and field-effect transistor structures. In addition, electric fields are an energetically higher perturbation, as compared with temperature and magnetic field, enough to cause electrostrain[6], induce ionic conduction[7], produce ferroelectric–non-ferroelectric transitions in quantum paraelectric materials and relaxor ferroelectrics[8,9], change the electronic state[10] and to electrostatically modulate correlated electron behaviour including high-temperature superconductivity and colossal magnetoresistance[11,12].

Here, we present the quasi-non-volatile and reversible modulation of electric conduction accompanied by the modulation of the ferroelectric state in Ca-doped $BiFeO_3$ films, using an electric field as the control parameter. The mechanism of this modulation in Ca-doped $BiFeO_3$ is based on electronic conduction as a consequence of the naturally produced oxygen vacancies that act as donor impurities to compensate calcium acceptors and maintain a highly stable Fe^{3+} valence state[13]. The interplay of ionic and electronic conduction is discussed in terms of the underlying cause for the observed conduction modulation behaviour.

The parent compound $BiFeO_3$ is one of the most actively studied multiferroic[14–16] thin-film materials. Its ferroelectric Curie temperature is ∼1,103 K (ref. 17) and the antiferromagnetic Néel temperature is ∼640 K (ref. 18). Bulk crystals have a rhombohedral symmetry (space group $R3c$); however, in thin films, strain induced by heteroepitaxy lowers the symmetry to monoclinic[19]. Regarding electric conduction, we would like to note that a hydrostatic-pressure-induced metal–insulator transition in $BiFeO_3$ single crystals has been reported[20], and that recent investigations of conductivity at domain walls[21] and the optical gap at high temperatures[22] suggest the possibility of stabilizing some conducting states in these compounds. Recently, divalent-ion doping effects on $BiFeO_3$ have been studied[23–25], but a consensus on the associated phase diagram has not yet been reached. We show that this phase diagram information is essential to implement the electric modulation of conduction and ferroelectric states by choosing an optimized doping ratio.

Our work investigates the phase diagram of the $Bi_{1-x}Ca_xFeO_{3-\delta}$ films as a function of the Ca doping concentration (x) and temperature through structural analysis (Fig. 1a). For the low Ca doping regime ($x < 0.1$), films with a monoclinic structure undergo a first-order transition to a pseudo-tetragonal phase at higher temperatures with a thermal hysteresis (Fig. 1b; see also Supplementary Information). The extrapolation of the transition temperature results in the well-known ferroelectric Curie temperature (T_c) of $BiFeO_3$ at ∼1,100 K. With increasing Ca doping, the ferroelectric T_c rapidly decreases, and a T_c of ∼600 K with a thermal hysteresis of 240 K is recorded at $x = 0.1$. It has been reported that the T_c of some ferroelectrics, such as $BaTiO_3$ and $PbTiO_3$, is very sensitive to the strain state[26,27]. However, because the ferroelectricity of $BiFeO_3$ is primarily attributed to the Bi 6s lone-pair electrons, the ferroelectric properties and the T_c are expected to be less sensitive to strain[28]. The samples in this doping regime ($x \leqslant 0.1$) show a clear piezoelectric domain structure, indicating ferroelectric long-range order, as imaged through piezoresponse force microscopy (PFM) studies. For the doping regime $x > 0.15$, the crystal structure exhibits a

[1]Department of Physics, University of California, Berkeley, California 94720, USA, [2]Materials Sciences Division, Lawrence Berkeley National Laboratory, California 94720, USA, [3]Department of Material Science and Engineering, University of California, Berkeley, California 94720, USA, [4]Department of Material Science and Engineering, National Chiao Tung University, HsinChu 30010, Taiwan, [5]Center for Nanophase Materials Sciences, Oak Ridge National Laboratory, Tennessee 37831, USA. *e-mail: chyang@berkeley.edu.

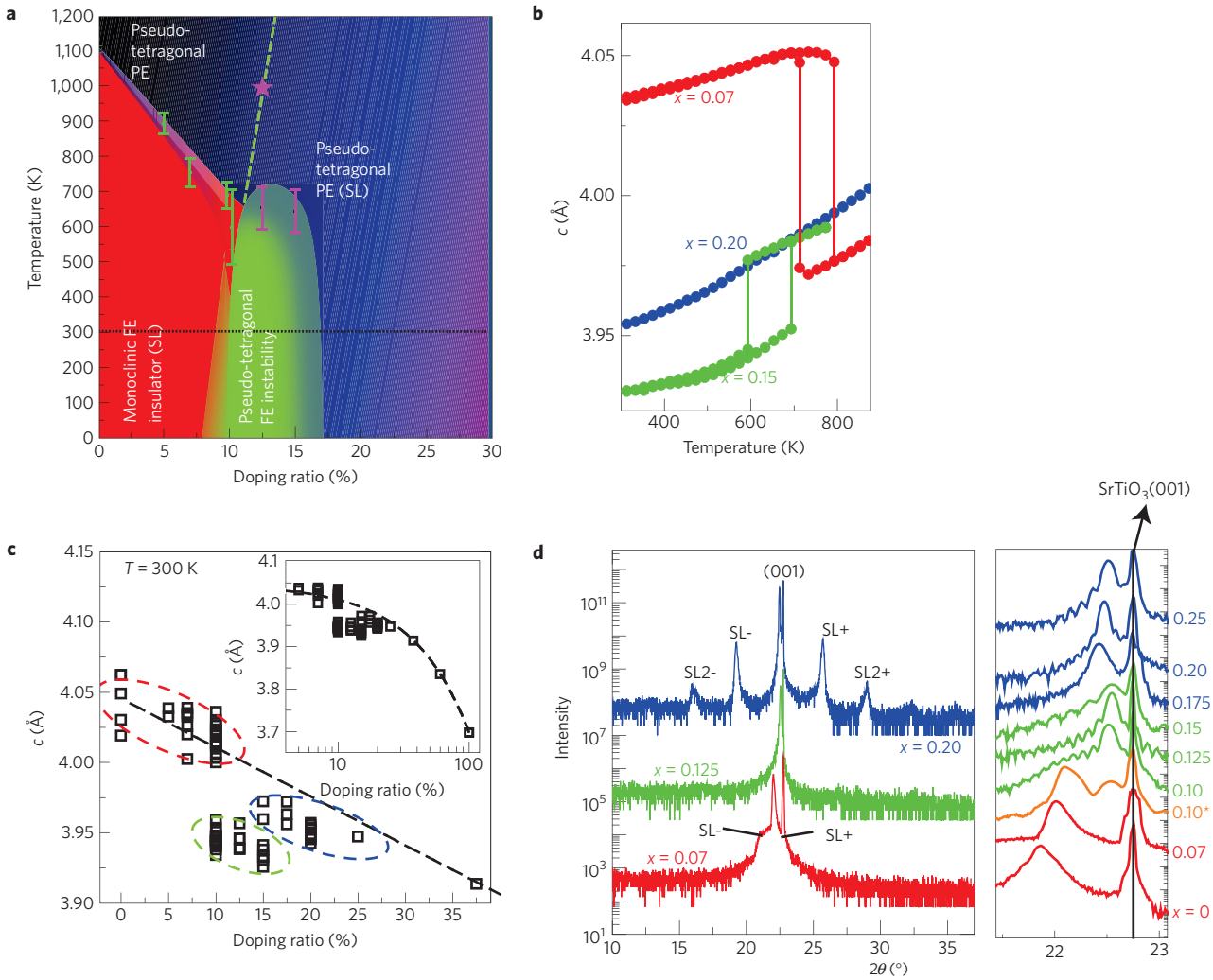

Figure 1 | Structural characterization of the Ca-doping effect on $BiFeO_3$ films. a, The proposed phase diagram of $Bi_{1-x}Ca_xFeO_{3-\delta}$ films grown on (001) $SrTiO_3$ substrates. A monoclinic ferroelectric (FE) state (red), pseudo-tetragonal paraelectric (PE) state (blue) and pseudo-tetragonal ferroelectric state (green) are present at room temperature, depending on the Ca doping ratio. The green- and magenta-coloured error bars indicate a thermal hysteresis due to a first-order transition between neighbouring phases. The green dashed line with a data point at high temperatures represents two different structural states of the paraelectric phase. The 'blue' phases on the right side exhibit superlattice peaks (as explained below); however the high-temperature phase on the left side does not exhibit superlattice peaks (like the green-coloured phase). The 'SL' in the phase diagram indicates the area showing the X-ray superlattice peak. **b**, The temperature dependence of the *c* axis lattice parameter is presented for the selected Ca concentrations. **c**, The Ca-substitution dependence of the *c* axis lattice parameter at room temperature. The data points collected from a library of 60 different samples are shown. The black dashed line denotes linear interpolation between the lattice parameter of $BiFeO_3$ and $CaFeO_{3-\delta}$ according to Vegard's law. The Ca doping between 10% and 15% results in a pseudo-tetragonal phase that has a considerably smaller *c* axis lattice parameter than the interpolation line and no structural modulation. At each phase boundary ($x \sim 0.1$ and 0.15), single or mixed phases composed of proximity phases can be stabilized within small uncertainties in the synthesis process. Inset: The same data are plotted on a logarithmic scale on the *x* axis and the dashed curve is the linearly interpolated Vegard's line. **d**, Left: Representative X-ray θ–2θ scans at room temperature of $Bi_{1-x}Ca_xFeO_{3-\delta}$ films at selected doping ratios. Films of $x = 0.20$ and 0.07 have superlattice peaks representing a structural modulation along the out-of-plane direction with a period of 7–8 unit-cells and ~24 unit-cells, respectively. The superlattice peaks become broader and are located closer to the (001) peaks with decreasing doping ratio; for $x = 0.07$, higher-order superlattice peaks are hardly observed, indicating a relatively weak ordering for the larger period of modulation. However, films of $x = 0.125$ do not have any superlattice peaks. Right: The existence of the superstructure is strongly related to the value of the *c* axis lattice parameter. The X-ray diffraction data around the (001) peak are shown for the films with a thickness (t) below 120 nm to reduce the possibility of strain relaxation: $t = 110$ nm (for $x = 0$), 100 nm ($x = 0.07$), 100 nm ($x = 0.10^*$), 100 nm ($x = 0.10$), 100 nm ($x = 0.125$), 60 nm ($x = 0.15$), 100 nm ($x = 0.175$), 120 nm ($x = 0.20$) and 80 nm ($x = 0.25$). The spectrum noted by $x = 0.10^*$ has two film peaks, implying coexistence of the 'red' and 'green' phases.

pseudo-tetragonal unit-cell, piezoelectricity is no longer detected and no anomalous change of the *c* axis lattice parameter is observed from room temperature to 1,100 K. In the intermediate doping regime, including concentrations around $x \sim 1/8$, the ferroelectric, monoclinic structure and the paraelectric, pseudo-tetragonal structure are no longer present, but a new pseudo-tetragonal phase is stabilized for the area described by the green colour in the phase diagram (Fig. 1a). Like the paraelectric phase above T_c, this phase has a smaller volume compared with the two neighbouring phases.

In Fig. 1c, the doping concentration dependence of the *c* axis lattice parameter at room temperature is shown. The dashed line represents a linear interpolation between the *c* axis lattice parameter of the $BiFeO_3$ films and that of $CaFeO_{3-\delta}$ films grown on (001) $SrTiO_3$ substrates. For most Ca concentrations

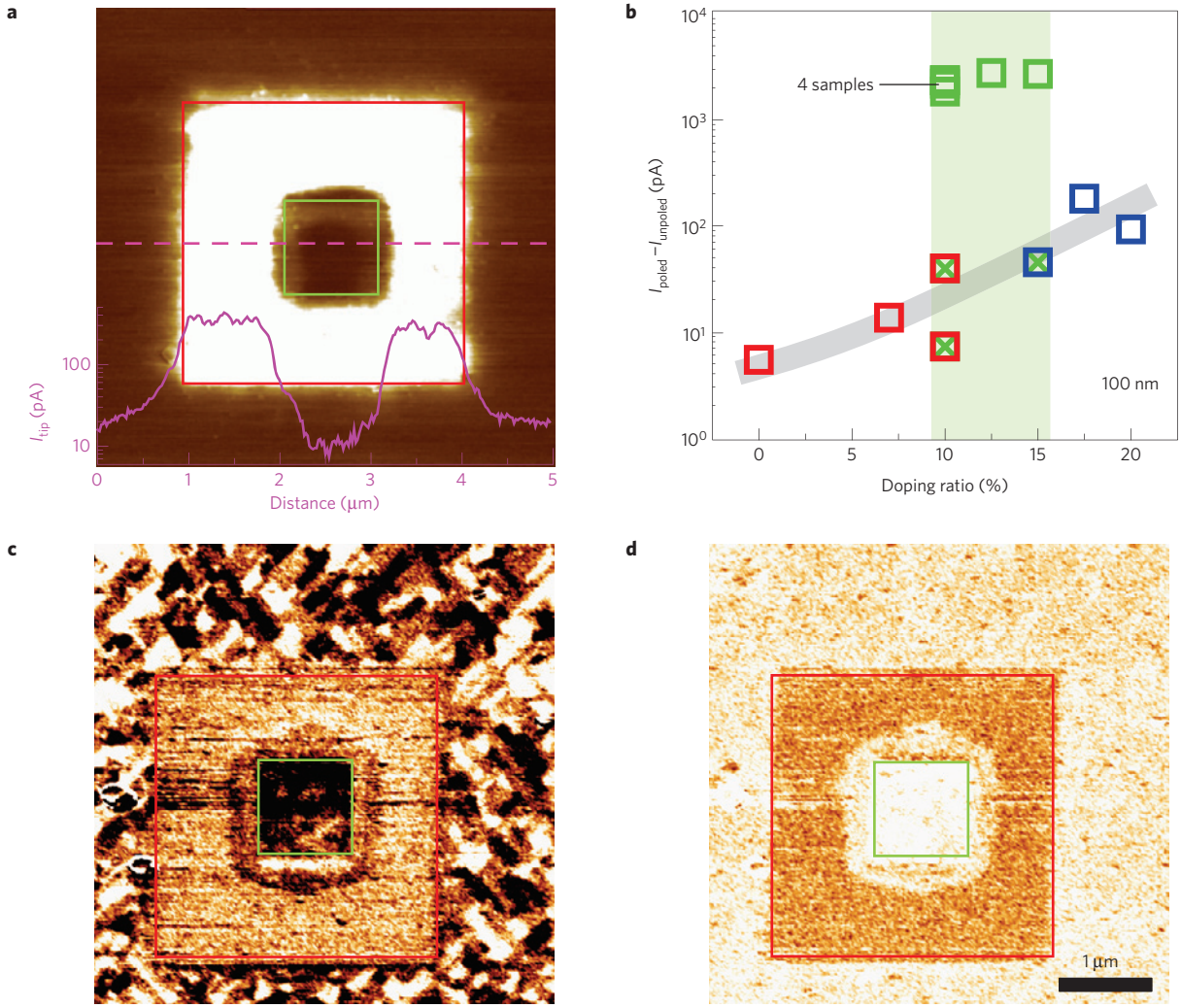

Figure 2 | Electric-field-driven phase transition between a ferroelectric, insulating state and a conducting state. a, Using the c-AFM technique, the local current with application of −2.5 V to the tip was measured for a $Bi_{0.8}Ca_{0.1}FeO_{3-\delta}$ film with a thickness of 300 nm over a $5 \times 5\,\mu m^2$ area after applying −12 V on a $3 \times 3\,\mu m^2$ area (red square) and sequentially poling with +12 V on a $1 \times 1\,\mu m^2$ area (green square). The bright region exhibits high current. Inset: The current profile along the magenta-coloured dashed line is plotted on a log scale. The conductivity change is as large as two orders of magnitude and it can be reset (conducting to insulating) by poling with positive voltages. **b**, The current enhancement by a negative poling is investigated, under the same measuring conditions, as a function of the Ca content in films with a thickness of 100 nm grown on a 50-nm-thick $SrRuO_3$ bottom electrode. The colours (red, green and blue) indicate the stabilized phases as explained in the phase diagram above and the 'x' on the data points implies the coexistence of neighbouring phases. The poling voltage of −12 V is applied over a $2 \times 2\,\mu m^2$ area and the c-AFM image is measured with −2 V over a $4 \times 4\,\mu m^2$ area. A tip speed of $1.5\,\mu m\,s^{-1}$ is used for the poling and measuring process, and the sensitivity of the c-AFM is set to $1\,V\,nA^{-1}$. **c**, In-plane PFM image over the poling area in which an electric field is applied as explained above. The high-conducting-state region has lost the domain contrast, showing monotonic brown colour, which means little or no piezoresponse. On the other hand, the as-grown state region outside the red square shows clear domains, implying a ferroelectric state similar to $BiFeO_3$. Inside the green square, large piezoresponse (in dark contrast) is observed, proving that the ferroelectric state is recovered. **d**, Out-of-plane PFM image over the poling area.

from $x = 0$ to 1, the c axis lattice parameters are located around the dashed line and only the $x \sim 1/8$ region shows a large deviation from a classical Vegard's law behaviour. This smaller c axis lattice parameter is not due to strain relaxation; X-ray reciprocal space mapping for the 203 diffraction peak confirms the in-plane lattice is fully strained to the substrate (see Supplementary Information). The possibility of volume reduction arising from extrinsic effects such as bismuth volatility can be excluded because the phase has been transformed reversibly into the paraelectric pseudo-tetragonal phase on raising the temperature (Fig. 1b).

Figure 1d shows X-ray θ–2θ scans for representative films from the three different doping regimes. For $x = 0.07$ and 0.20, superlattice peaks are observed around the 001 Bragg peak, indicating a structural modulation along the out-of-plane direction, which is probably due to an oxygen vacancy ordering as has been reported in perovskite-related ferrites[29–31]. Interestingly, the phase with the smaller volume located at the boundary between the ferroelectric and non-ferroelectric phases does not show superlattice peaks. This correlation between the c axis lattice parameter and the existence of the superstructure can also be identified in the high-temperature transition observed in the film with $x = 0.15$ (see Supplementary Information). The increase of the c axis lattice parameter measured above ~650 K (for $x = 0.15$) is mainly due to this appearance of the superstructure accompanying the paraelectric state. This experimental observation suggests that an oxygen vacancy ordering could be another degree of freedom that is inter-coupled in this system.

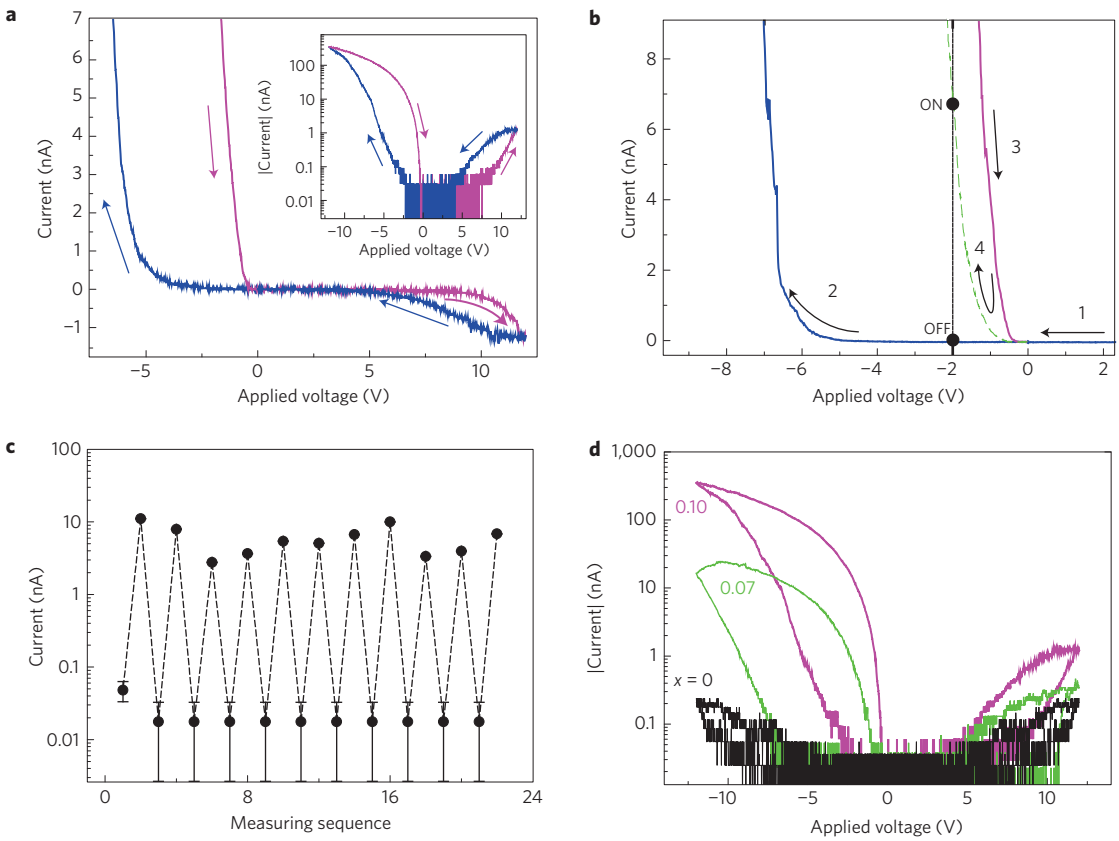

Figure 3 | Local current (*I*)–voltage (*V*) characteristics. a, Hysteric behaviour of the *I*–*V* curve provides a viable route to a resistive switching memory for a $Bi_{0.8}Ca_{0.1}FeO_{3-\delta}$ film with a thickness of 100 nm. The voltage relatively applied to the tip is swept sequentially from 0 V to −12 V, and from −12 V to 12 V, and from 12 V to 0 V, at a rate of 0.18 V s^{-1}, and the *I*–*V* curve is plotted linearly and logarithmically (inset). **b**, ON/OFF states at the reading voltage of −2 V can be set by applying two high (∓12 V) voltages. The numbers inside the rectangles denote the sequence of voltage sweeps. After returning from +12 V, a high resistance state at −2 V is measured (OFF state), whereas after returning from −12 V, low resistance is obtained (ON state). **c**, This hysteric switching behaviour is repeatedly measured. The current level at −2 V is monitored while cycling the sweep. **d**, The Ca doping dependence of *I*–*V* hysteresis. On increasing the doping ratio, larger ON/OFF switching ratios are obtained.

On the basis of the structural characterization, we focus on the pseudo-tetragonal ferroelectric phase (green-coloured region in the phase diagram) at $x = 0.10$ as a suitable composition to investigate the electric modulation of conducting and ferroelectric states. We choose this phase because it is located near the phase boundary, which may make it susceptible to external electric fields in terms of both ferroelectricity and electric conduction, whereas for $x < 0.1$ the electric conduction is not high enough and for $x > 0.15$ the ferroelectric state is not stabilized.

The local electrical conductivity of a 300-nm-thick film grown on a $SrRuO_3$ (50 nm thick) bottom electrode by pulsed laser deposition (see the Methods section) was probed by conducting-atomic force microscopy (c-AFM). Using a conducting tip, micrometre-sized regions of the film were electrically switched with a set of positive and negative voltages (Fig. 2a). A 3 μm region was poled with a voltage of −12 V (red square), inside which a smaller 1 μm region was subsequently poled downward with a voltage of +12 V (green square). For these regions, local currents were measured by the c-AFM technique with a voltage of −2.5 V. The region poled with −12 V shows a large increased local conductivity that can be switched back to the insulating state by applying a downward field of +12 V. The line profile of the c-AFM image plotted (on a log scale in pink) reveals that the conducting state leads to a few hundred picoamperes of current that is modulated by at least two orders of magnitude. This observed contrast is repeatable over the same region as well as other regions of the sample; measurements were carried out in three other samples, with results that were similar to that shown in Fig. 2. The slow relaxation of the high current state can be probed in thinner films (thickness ∼100 nm) within a reasonably measurable timescale. Such retention studies show that the enhanced conduction in the poled region lasts more than 36 h, but becomes diffuse after one week (for details, see Supplementary Information). On the basis of Fick's second law and the assumption that the inter-diffusion length for one week is of the order of the film thickness (∼100 nm), the diffusivity ($\mathcal{D}$) of oxygen vacancies can be estimated to be $\sim 10^{-17}$ cm^2 s^{-1}. This is a reasonable value for the oxygen vacancy movement in non-stoichiometric perovskites and related compounds[32–34]. Figure 2b summarizes the change in this conductance with electric field (plotted as the difference between measured current in the poled and unpoled states) as a function of doping concentration. It is interesting to note that the concentration regime (shaded green in Fig. 1a) that shows the large deviations in lattice parameters is also the one that exhibits the largest conductance modulation.

To study the involvement of the ferroelectric state, PFM measurements for the same sample were carried out over the region poled using the same method described above (Fig. 2c). The region outside the poling area shows clear ferroelectric domains, indicating that this Ca-doped (10%) sample is ferroelectric. The three shades of image contrast, namely white, black and brown, found in this region of the PFM image indicate different directions of the polarization projected in-the-plane of the film, which are typical for $BiFeO_3$ films grown on (001) $SrTiO_3$ substrates[35]. Similarly, in

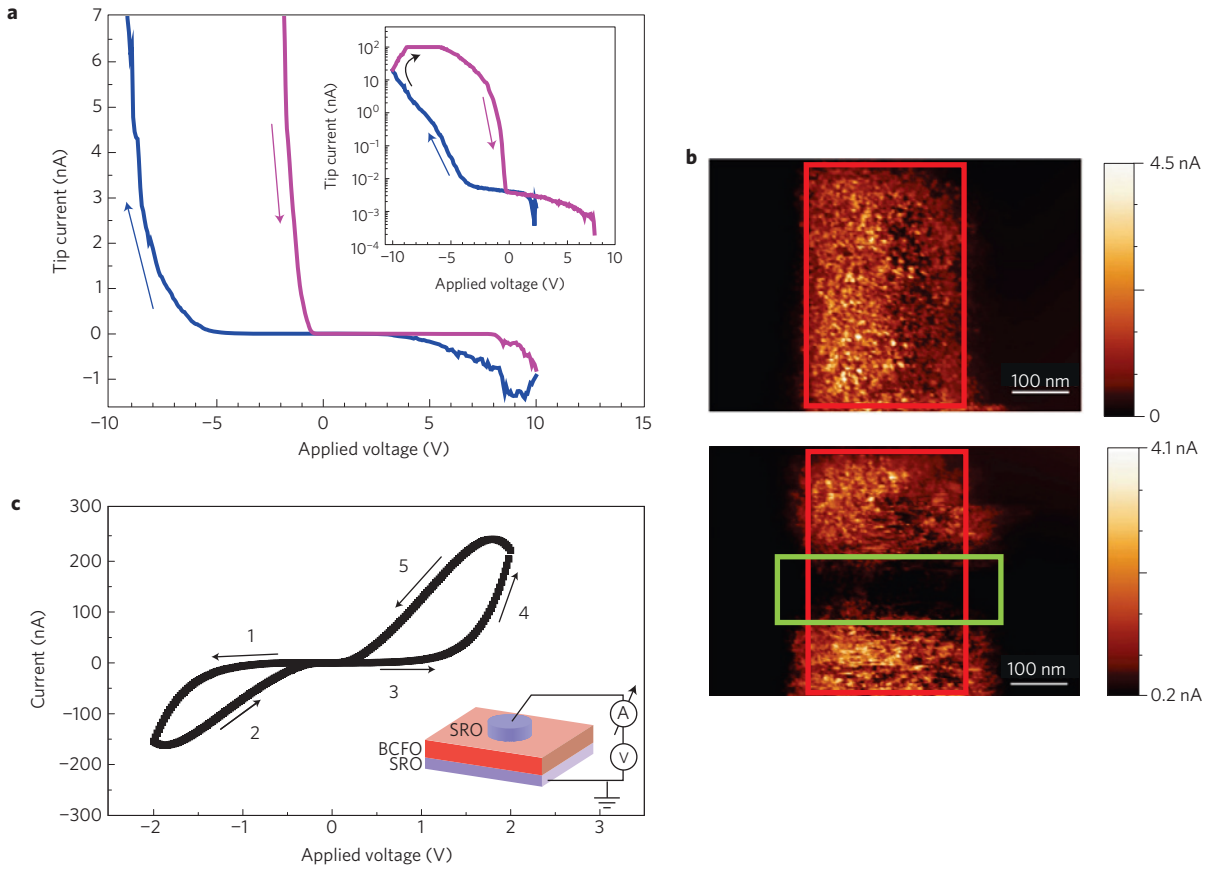

Figure 4 | Reproducing the electronic conduction switching in ultrahigh vacuum c-AFM measurement and in the conventional capacitor geometry. **a**, Local *I*–*V* measurement carried out for the $Bi_{0.8}Ca_{0.1}FeO_{3-\delta}$ film (100 nm in thickness). A local high conducting state and a diode-like *I*–*V* characteristic appear after a high negative voltage (>−8 V) is applied to the tip. The *I*–*V* curve is acquired by sweeping the tip bias from +10 to −10 V and back to +10 V, at a rate of 0.6 V s^{-1}. Inset: The same *I*–*V* curve on a logarithmic scale. **b**, Top: The current image over an area poled at a tip voltage of −10 V (inside red rectangle). Bottom: The area in the top panel after applying a tip voltage of +6 V inside the green rectangle. Both current images are measured with a tip voltage of −6 V. The rate of tip motion during poling and measurement was 0.6 μm s^{-1}. **c**, The resistive switching behaviour in the conventional capacitor geometry. The tri-layers of $SrRuO_3$ (50 nm)/$Bi_{0.9}Ca_{0.1}FeO_{3-\delta}$ (100 nm)/$SrRuO_3$ (50 nm) are *in situ* epitaxially grown. Through a photolithography and ion milling technique, we have made the top $SrRuO_3$ electrode with a diameter of 20 μm, as shown in the inset. The *I*–*V* curve is acquired by sweeping the voltage of the top electrode (0 → −2 V → +2 V → 0 V as indicated by the number inside the rectangles), at a rate of 20 mV s^{-1}.

the region poled with +12 V (green square), strong piezoresponse (black colour) and a black/brown contrast was detected, implying that the ferroelectric state has been recovered. On the contrary, in the highly conducting region, no domain structure is observed and the brown tone in the PFM image is indicative of weak or no piezoresponse. The out-of-plane PFM (Fig. 2d) also shows weak piezoresponse (brown colour) in the conducting area but the as-grown region and the region poled with +12 V exhibit white colour, which implies the out-of-plane polarization direction is downward directed. These observations can be understood by the fact that the enhanced conductivity frustrates ferroelectric order by screening long-range Coulomb interaction, which has a key role in stabilizing the cooperative alignment of dipole moments[36].

Figure 3 shows detailed current (I)–voltage (V) characteristics of the modulation in the transport properties. Clear I–V hysteresis is observed and is replicated reversibly. On application of a high negative bias to the AFM tip with respect to the bottom electrode, the current is significantly increased with a nonlinear feature around a threshold voltage of ∼−6 V and reaches 350 nA at a voltage of −12 V through the conducting diamond tip. If it is assumed that the effective contact area of the tip on the sample surface is circular with a diameter of 50 nm, the conductivity at a voltage of −12 V corresponds to approximately $1.5 \times 10^{-2}\,(\Omega\,\mathrm{cm})^{-1}$, which is indicative of a semiconducting transport regime. Even though a high oxygen vacancy density (n_{Vo}) of $8 \times 10^{20}\,\mathrm{cm}^{-3}$ is expected for $x = 0.1$ under the constraint of charge neutrality and a nearly fixed valence state of Fe^{3+}, the ionic conductivity estimated by the Nernst–Einstein relation,

$$\sigma_{\mathrm{ion}} = \frac{n_{\mathrm{Vo}} e^2 \mathcal{D}}{k_{\mathrm{B}} T}$$

is less than $10^{-13}\,(\Omega\,\mathrm{cm})^{-1}$ for the case of a diffusivity ($\mathcal{D}$) of $10^{-17}\,\mathrm{cm}^2\,\mathrm{s}^{-1}$ at room temperature. This huge difference between the measured conductivity and the estimated ionic conductivity suggests that the main carrier type leading to the observed transport behaviour must be electronic rather than ionic in nature. The I–V curve shape is changed to a diode-like behaviour after applying high electric fields. For the conducting state to return to the insulating state, a high positive voltage has to be applied; otherwise, the current still exhibits a high value at a voltage of −2 V (Fig. 3b). This hysteric I–V shape can potentially be used for a resistive memory device; for instance, two different current states at −2 V could represent ON/OFF states, respectively. Figure 3c presents the repeatability of the ON/OFF switching by cycling the full hysteresis. This modulation becomes smaller at $x = 0.07$ and eventually no large effect is observed in pure $BiFeO_3$ films (Fig. 3d).

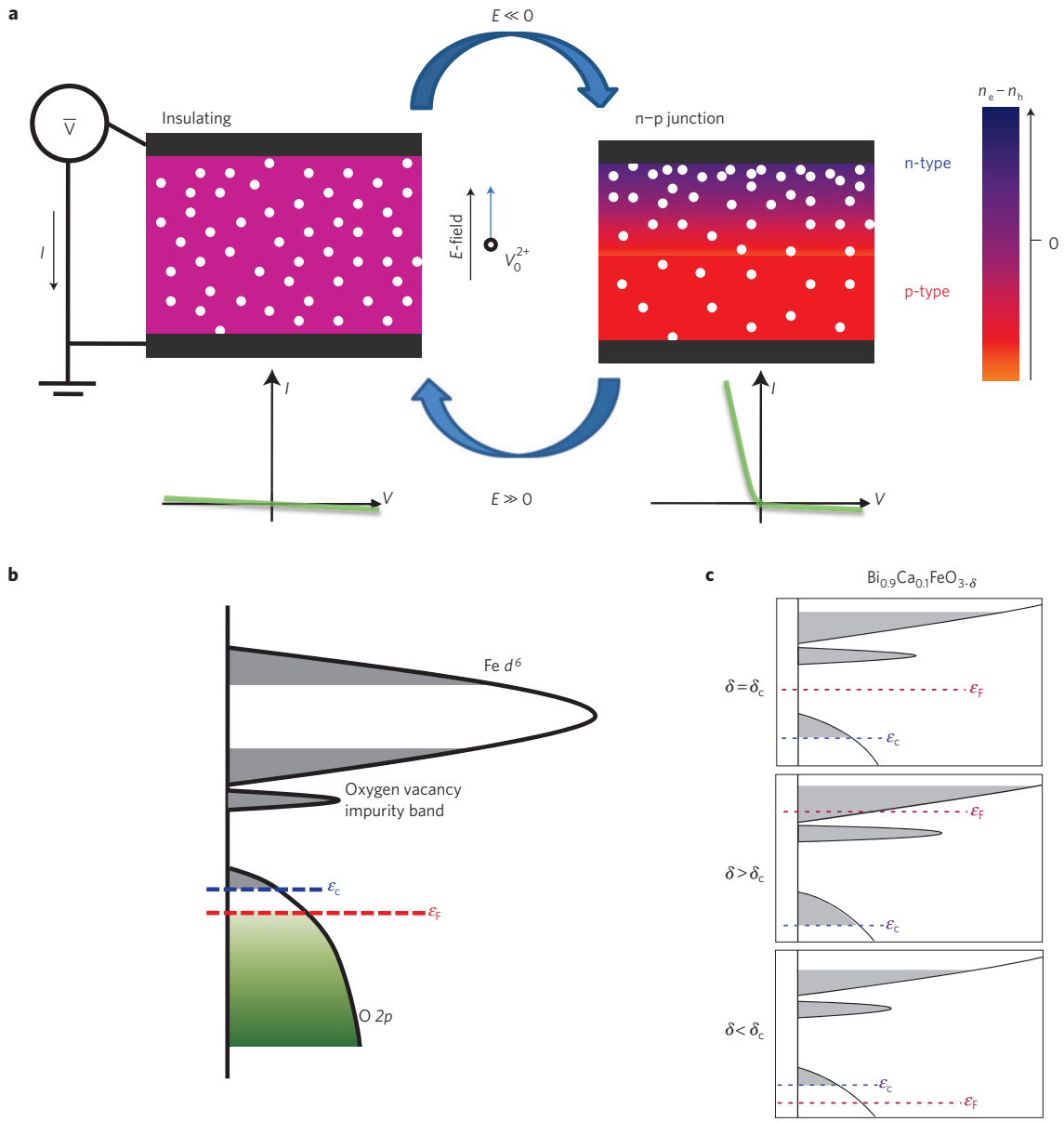

Figure 5 | The mechanism of the electronic conduction switching. a, Schematic diagram describing the switching mechanism of electronic states in $Bi_{1-x}Ca_xFeO_{3-\delta}$ films. Oxygen vacancies are spontaneously produced to compensate hole carriers and to maintain the valence state of Fe^{3+}. This highly insulating state is thermodynamically stable. The oxygen vacancies respond to electric field in this ionic conductor because the oxygen vacancies are positively charged as a consequence of their ionization. In a negative field (bottom to top directional field), oxygen vacancies are moving upward and accumulating near the top surface and are frozen when the field is turned off. As a result, a state with n-type carriers is realized, locally in the donor accumulating region; the opposite region becomes a p-type conductor. By applying an opposite, high electric field, the inhomogeneous donor distribution can be reversed to an evenly distributed insulating state. **b**, Schematic diagram of the electronic density of states. The insulator–conductor transition happens locally when the Fermi energy (ε_F), which is controlled by the oxygen vacancy concentration (n_{V_O}), passes across the mobility edge (ε_c). The band edges (grey-coloured regions) are composed of localized states with low mobility owing to inherent randomness in this system as a result of Anderson localization. **c**, The band-filling at representative oxygen vacancy ratios (δ). δ_c stands for a critical ratio to compensate exactly hole carriers produced by calcium acceptors. The value of δ_c corresponds to 0.05 for $x = 0.10$ as an oxygen vacancy is regarded as a double electron donor.

To exclude the possibility of surface contamination as the possible reason for the observed change in conductivity, we carried out local I–V measurements and current imaging of the poled area in an ultrahigh vacuum environment. As shown in Fig. 4a,b, the characteristic I–V curve and the writing/erasing process that was observed in the ambient measurements are reproduced. In addition, we fabricated a conventional capacitor structure using an epitaxially grown tri-layer of $SrRuO_3$ (50 nm)/$Bi_{0.9}Ca_{0.1}FeO_{3-\delta}$ (100 nm)/$SrRuO_3$ (50 nm) to eliminate possible effects of Schottky contact resistance at the interface between the tip and ferroelectric film[37]. The electric-field-driven resistance switching behaviour has been reproduced in this structure as well (see Fig. 4c).

We now focus on the origin of the modulation of electric conduction. We hypothesize that the oxygen vacancies created to maintain charge neutrality are critical to understand the conduction behaviour as illustrated schematically in Fig. 5a. Ionization of oxygen vacancies in Ca-doped $BiFeO_3$ yields electrons to compensate hole carriers introduced by the Ca to maintain the 3+ valence state of the iron ions. Provided that the oxygen vacancies

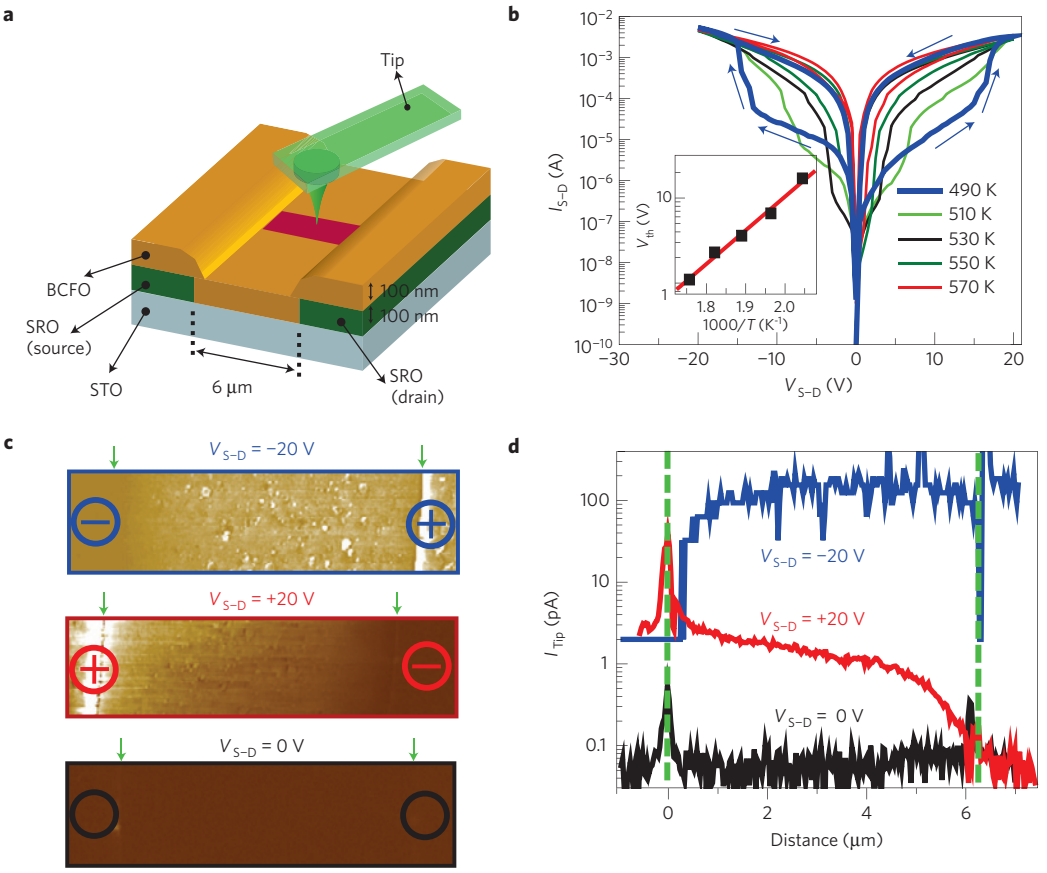

Figure 6 | Controlling oxygen vacancy concentration in-plane. a, Schematic diagram of the planar electrode structure. **b**, *I*–*V* measurement at selected temperatures using source and drain electrodes. Inset: Arrhenius plot of the threshold voltage. The activation energy calculated from the slope of the linear fit is 0.76 eV. **c**, The film is heated to 473 K and $V_{S-D} = -20$ V is applied so that oxygen vacancies move towards the source and accumulate there. After monitoring that I_{S-D} is significantly increased, the temperature is quickly dropped to room temperature. Then, c-AFM measurements with a tip voltage of −1.5 V are carried out for the quenched-in state (top panel). Similarly, the opposite field effect is investigated (middle panel). The twin electrode structure, fabricated in the same film, is just heated without the poling and measured as a reference to check the thermal annealing effect (bottom panel). The green arrows indicate the side walls of the electrodes. The images are independent of the tip sweeping direction and speed. For $V_{S-D} = -20$ V, a low sensitivity setting was used. Both the source and drain electrodes are electrically at the same potential when the c-AFM measurement is carried out. **d**, The horizontal profiles for the c-AFM results.

are mobile positive charges, they can move through the sample under electric fields to find a new thermodynamic equilibrium[38,39]. For example, oxygen vacancies can move and pile up near the top surface for negative bias conditions. As a result, the donor oxygen vacancies and the acceptor calcium ions are locally unbalanced; thus, the top surface region acquires n-type carriers, whereas the region near the bottom electrode becomes p-type. This electric-field-driven n–p junction explains the aforementioned diode-like *I*–*V* shape. Applying the opposite electric field moves oxygen vacancies to the original evenly distributed state, thus forming an electronic insulator. We would like to note that a positive electric field can be used to make the opposite diode structure; however, for the aforementioned c-AFM case, the effect of the positive field is not as large as that of the negative poling. This is due to an asymmetric response caused by a Schottky barrier between the tip and film leading to different voltage drops across the sample in different bias directions.

Another interesting question centres on why the measured current is abruptly enhanced at a threshold voltage despite the fact that, according to ohmic conduction of ionic transport, the oxygen vacancy distribution should be continuously varied by sweeping the applied voltage. This behaviour can be understood in terms of an electronic localization–delocalization transition through band-filling control. In other words, when the Fermi level (ε_F), controlled by the oxygen vacancy concentration, passes across a specific energy level, that is, the mobility edge (ε_c), an electronically conducting state appears locally (Fig. 5b,c). In principle, this mechanism is in effect for both n-type and p-type doping; however, in our case the mobility edge in the valence band is the critical criterion determining global conductance because oxygen vacancies thermodynamically are highly confined near the anode[40] and most of the region has hole carrier doping. So, globally a transition to the highly conducting state can be interpreted by the expansion of a locally highly conducting p-type region. The critical concentration (n_c), which is defined as the hole carrier concentration at the moment the Fermi energy meets the mobility edge, can be estimated by the Mott criterion[41,42]: $a_B n_c^{1/3} \sim 0.25$. The radius of bound hole states (a_B) is defined by the following:

$$a_B = \frac{4\pi\hbar^2\varepsilon}{m^* e^2}$$

where ε is the dielectric permittivity ($\varepsilon/\varepsilon_0 = 100$ for $BiFeO_3$; ref. 43) and m^* stands for the effective mass of hole carriers (m^*/m_0 is typically 5–20). Therefore, the critical concentration (n_c) is $\sim 1 \times 10^{19}$ to 8×10^{20} cm^{-3}. This concentration is comparable or less than the initial oxygen vacancy density ($n_{Vo} = 8 \times 10^{20}$ cm^{-3}),

suggesting that a conductor–insulator transition is attainable by reducing the oxygen vacancy density. Besides, n-type carriers tend to be strongly localized owing to the following two reasons: (1) oxygen vacancies lower the adjacent Fe 3*d* levels energetically, resulting in a localized impurity band located at 0.28 eV below the conduction band minimum[44] and n-type carriers must be trapped in this impurity band; (2) the conduction band is mainly composed of Fe t_{2g} orbitals. The hopping strength between neighbouring t_{2g} orbitals through π-bonding is not as large as Fe e_g and O 2*p* bands, thus resulting in a relatively large effective mass[45]. Therefore, the hallmark of this scenario is that there should be a boundary between conducting p-type region and insulating n-type region along the direction of electric field.

We probed this oxygen-vacancy-assisted electronic conduction mechanism, by measuring local conductivity for in-plane gradient distributions of oxygen vacancy created by a coplanar electrode structure, as shown in Fig. 6a. Films were poled under elevated temperatures to facilitate the insulator–conductor transition across the two electrodes separated by 6 μm within reasonable voltage ranges. The threshold voltage decreases with increasing temperature owing to the enhancement of σ_{ion} at higher temperature. As a result, the peculiar p–n/n–p junction characteristics and the threshold behaviour are reproduced in the *I*–*V* measurement for this planar electrode structure (Fig. 6b). We control the oxygen vacancy concentration distribution gradually between the two electrodes by applying +20 V to the source electrode for one minute at 473 K and sequentially by quenching to room temperature so that the distribution is frozen. As expected, c-AFM measurements (Fig. 6c,d) show a gradually varying current profile. The region near the source electrode is conducting owing to a high hole carrier density, whereas the opposite narrow region near the drain electrode reveals an insulating state because n-type carriers are localized as explained above. On the other hand, the application of −20 V to the source electrode makes the gradient profile reverse. The exclusion of side effects arising from the heating can be ascertained by the observation of no conductivity enhancement for an unpoled reference pattern fabricated on the same film. Finally, it is worthwhile to mention that the conducting areas can also be observed through optical microscopy (for the image of similarly poled area in-plane, see Supplementary Information).

In summary, the effect of divalent-ion-calcium doping on multiferroic $BiFeO_3$ films was investigated and a phase diagram was built by varying the doping concentration and temperature. A ferroelectric–paraelectric boundary exists at doping levels of $x \sim 1/8$, stabilizing a pseudo-tetragonal phase that has a relatively smaller volume than that expected from Vegard's law. We have also studied the electric conduction of these films, applying electric field along both the normal and in-plane directions. In both cases, electronic conduction can be modulated in a similar way. The mechanism discussed is based on the interplay of ionic and electronic conduction. We argue that application of an electric field can be a promising route to effectively 'sweep' oxygen vacancies to one side of the device preferentially and thus induces a transition to a conducting state in $Bi_{1-x}Ca_xFeO_{3-\delta}$ films. These conductor–insulator transitions can be understood in terms of the competition between a mobility edge and Fermi energy through band-filling control.

Methods

Ca-doped $BiFeO_3$ films were grown on (001) $SrTiO_3$ substrates using pulsed laser deposition at 600–700 °C in 50–100 mtorr oxygen pressure. Typical deposition rates were approximately 2 nm min^{-1} with a laser repetition rate of 10 Hz. The pulsed KrF excimer laser (wavelength 248 nm) was focused to reach a laser fluence of ∼2 J cm^{-2} on the target surface. The films were cooled down at a rate of 5 °C min^{-1} with ∼1 atm oxygen pressure. For electrical measurements along the out-of-plane direction, a conducting $SrRuO_3$ layer (∼50 nm in thickness) was pre-grown as a bottom electrode. The crystal structures were investigated by X-ray diffraction (Panalytical X'Pert MRD Pro) with Cu $K_{\alpha 1}$ radiation. The thickness of films is determined by X-ray reflectivity measurement and by analysing the Kiessig fringes around the (00L) Bragg peak. For the investigation at high temperatures, a commercial heating stage (DHS-900) was used. The θ–2θ scans for the (002) peak were measured every 20 K. Each θ–2θ measurement takes ∼10 min after temperature stabilization during ∼5 min. These high-temperature measurements were carried out in air.

Local piezoelectric and local conductivity properties, under ambient conditions, were studied by an AFM-based set-up. Nanoscale conductivity measurements were carried out on a Digital Instruments Nanoscope-IV Multimode AFM equipped with a conductive AFM application module. Using conductive AFM tips, it is possible to measure local electrical and topographical properties both simultaneously and independently. The investigations were carried out with commercially available nitrogen-doped diamond-coated Si tips (NT-MDT). The PFM image was acquired on the same Multimode system using TiPt-coated Si tips (MikroMasch). Typical scan rates were 1.5 μm s^{-1}. For the c-AFM measurement in ultrahigh vacuum, a customized scanning force microscope (Omicron VT-STM/AFM) was used for measurements at a pressure of 2×10^{-10} torr. Current was measured in contact mode, using a preamplifier directly connected to the tip through a shielded cable. The measurements were carried out using Au-coated tips (CSC37 from MikroMasch).

The coplanar electrode structures are fabricated by first growing epitaxial conducting $SrRuO_3$ films on (001) $SrTiO_3$ substrates (∼100 nm in thickness) at 700 °C. Photolithography is used to define the area of source and drain electrodes (∼50 μm wide and separated by a 6 μm gap). Then, the surrounding area except for the defined area is etched by ion milling down to the underlying substrates. Following this process, Ca-doped (10%) $BiFeO_3$ film with a thickness of 100 nm is grown on the patterned substrate. The *I*–*V* curve for this planar electrode structure is measured using a Keithley multimeter (Model 2000) with a sweeping speed of 0.65 V s^{-1}.

Received 15 October 2008; accepted 20 March 2009; published online 26 April 2009

References

1. Imada, M., Fujimori, A. & Tokura, Y. Metal–insulator transitions. *Rev. Mod. Phys.* **70**, 1039–1263 (1998).
2. Jin, S. *et al.* Thousandfold change in resistivity in magnetoresistive La–Ca–Mn–O films. *Science* **264**, 413–415 (1994).
3. Uehara, M., Mori, S., Chen, C. H. & Cheong, S. W. Percolative phase separation underlies colossal magnetoresistance in mixed-valent manganites. *Nature* **399**, 560–563 (1999).
4. Verwey, E. J. W. Electronic conduction of magnetite (Fe_3O_4) and its transition point at low temperatures. *Nature* **144**, 327–328 (1939).
5. Liu, Y., Haviland, D. B., Nease, B. & Goldman, A. M. Insulator-to-superconductor transition in ultrathin films. *Phys. Rev. B* **47**, 5931–5946 (1993).
6. Ren, X. Large electric-field-induced strain in ferroelectric crystals by point-defect-mediated reversible domain switching. *Nature Mater.* **3**, 91–94 (2004).
7. Agrawal, R. C. & Gupta, R. K. Superionic solids: Composite electrolyte phase—an overview. *J. Mater. Sci.* **34**, 1131–1162 (1999).
8. Hemberger, J. *et al.* Quantum paraelectric and induced ferroelectric states in $SrTiO_3$. *J. Phys. Condens. Matter* **8**, 4673–4690 (1996).
9. Xu, G., Zhong, Z., Bing, Y., Ye, Z.-G. & Shirane, G. Electric-field-induced redistribution of polar nano-regions in a relaxor ferroelectric. *Naure Mater.* **5**, 134–140 (2006).
10. Meijer, G. I. *et al.* Valence states of Cr and the insulator-to-metal transition in Cr-doped $SrTiO_3$. *Phys. Rev. B* **72**, 155102 (2005).
11. Ahn, C. H., Triscone, J.-M. & Mannhart, J. Electric field effect in correlated oxide systems. *Nature* **424**, 1015–1018 (2003).
12. Ahn, C. H. *et al.* Electricstatic modification of novel materials. *Rev. Mod. Phys.* **78**, 1185–1212 (2006).
13. Yamamura, H. & Kiriyama, R. Oxygen vacancies in the perovskite-type ferrites. I. Relation between oxygen vacancies and structures in the solid solution systems $Sr_{1-x}M_xFeO_{3-\delta}$ (M = yittrium, lanthanum, bismuth, and indium). *Nippon Kagaku Kaishi* **2**, 343–349 (1972).
14. Fiebig, M. Revival of the magnetoelectric effect. *J. Phys. D* **38**, R123–R152 (2005).
15. Ramesh, R. & Spaldin, N. A. Multiferroics: Progress and prospects in thin films. *Nature Mater.* **6**, 21–29 (2007).
16. Cheong, S. W. & Mostovoy, M. Multiferroics: A magnetic twist for ferroelectricity. *Nature Mater.* **6**, 13–20 (2007).
17. Roginska, Y. E., Tomashpo, Y. Y., Venevtse, Y. N., Petrov, V. M. & Zhdanov, G. S. Nature of dielectric and magnetic properties of $BiFeO_3$. *Sov. Phys. JETP* **23**, 47–51 (1966).
18. Kiselev, S. V., Ozerov, R. P. & Zhdanov, G. S. Detection of magnetic order in ferroelectric $BiFeO_3$ by neutron diffraction. *Sov. Phys. Dokl.* **7**, 742–744 (1963).
19. Chu, Y. H. *et al.* Domain control in multiferroic $BiFeO_3$ through substrate vicinality. *Adv. Mater.* **19**, 2662–2666 (2007).

20. Gavriliuk, A. G. *et al.* Another mechanism for the insulator–metal transition observed in Mott insulators. *Phys. Rev. B* **77**, 155112 (2008).
21. Seidel, J. *et al.* Conduction at domain walls in oxide multiferroics. *Nature Mater.* **8**, 229–234 (2009).
22. Palai, R. *et al.* β phase and γ–β metal–insulator transition in multiferroic $BiFeO_3$. *Phys. Rev. B* **77**, 014110 (2008).
23. Brinkman, K., Iijima, T. & Takamura, H. Acceptor doped $BiFeO_3$ ceramics: A new material for oxygen permeation membranes. *Japan. J. Appl. Phys. 2* **46**, L93–L96 (2007).
24. Khomchenko, V. A. *et al.* Synthesis and multiferroic properties of $Bi_{0.8}A_{0.2}FeO_3$ (A = Ca, Sr, Pb) ceramics. *Appl. Phys. Lett.* **90**, 242901 (2007).
25. Li, J., Duan, Y., He, H. & Song, D. Crystal structure, electronic structure, and magnetic properties of bismuth-strontium ferrites. *J. Alloys Compounds* **315**, 259–264 (2001).
26. Pertsev, N. A., Zembilgotov, A. G. & Tagantsev, A. K. Effect of mechanical boundary conditions on phase diagrams of epitaxial ferroelectric thin films. *Phys. Rev. Lett.* **80**, 1988–1991 (1998).
27. Schlom, D. G. *et al.* Strain tuning of ferroelectric thin films. *Annu. Rev. Mater. Res.* **37**, 589–626 (2007).
28. Ederer, C. & Spaldin, N. A. Effect of epitaxial strain on the spontaneous polarization of thin film ferroelectrics. *Phys. Rev. Lett.* **95**, 257601 (2005).
29. Klie, R. F. & Browning, N. D. Characterization of oxygen ordering in $(La,Sr)FeO_{3-\delta}$ by atomic resolution Z-contrast imaging and electron energy-loss spectroscopy. *J. Electron Microscopy* **51**, S59–S66 (2002).
30. Becerro, A. I. *et al.* The transition from short-range to long-range ordering of oxygen vacancies in $CaFe_xTi_{1-x}O_{3-x/2}$ perovskites. *Phys. Chem. Chem. Phys.* **2**, 3933–3941 (2000).
31. Grenier, J.-C., Pouchard, M. & Hagenmuller, P. Vacancy ordering in oxygen-deficient perovskite-related ferrites. *Struct. Bond.* **47**, 1–25 (1981).
32. Vashook, V. V., Daroukh, M. A. & Ullmann, H. Oxygen ion diffusion in perovskite-type oxides determined by permeation and by relaxation measurements. *Ionics* **7**, 59–66 (2001).
33. Mogilevsky, R. *et al.* Direct measurements of room-temperature oxygen diffusion in $YBa_2Cu_3O_x$. *Phys. Rev. B* **49**, 6420–6423 (1994).
34. Merkle, R. & Maier, J. How is oxygen incorporated into oxides? A comprehensive kinetic study of a simple solid-state reaction with $SrTiO_3$ as a model material. *Angew. Chem. Int. Ed.* **47**, 3874–3894 (2008).
35. Zavaliche, F. *et al.* Ferroelectric domain structure in epitaxial $BiFeO_3$ films. *Appl. Phys. Lett.* **87**, 182912 (2005).
36. Uchida, K., Tsuneyuki, S. & Schimizu, T. First principles calculations of carrier-doping effects in $SrTiO_3$. *Phys. Rev. B* **68**, 174107 (2003).
37. Blom, P. W. M., Wolf, R. M., Cillessen, J. F. M. & Krijn, M. P. C. M. Ferroelectric Schottky diode. *Phys. Rev. Lett.* **73**, 2107–2110 (1994).
38. Bunget, I. & Popescu, M. *Physics of Solid Dielectrics* (Elsevier, 1984).
39. Szot, K., Speier, W., Bihlmayer, G. & Waser, R. Switching the electric resistance of individual dislocations in single-crystal $SrTiO_3$. *Nature Mater.* **5**, 312–320 (2006).
40. Clayton, J. D., Chung, P. W., Grinfeld, M. A. & Nothwang, W. D. Continuum modeling of charged vacancy migration in elastic dielectric solids, with application to perovskite thin films. *Mech. Res. Commun.* **35**, 57–64 (2008).
41. Mott, N. F. Metal–insulator transition. *Rev. Mod. Phys.* **40**, 677–683 (1968).
42. Tsuda, N., Nasu, K., Yanase, A. & Siratori, K. *Electronic Conduction in Oxides* (Springer, 2000).
43. Lim, S.-H. *et al.* Enhanced dielectric properties in single crystal-like $BiFeO_3$ thin films grown by flux-mediated epitaxy. *Appl. Phys. Lett.* **92**, 012918 (2008).
44. Hauser, A. J. *et al.* Characterization of electronic structure and defect states of thin epitaxial $BiFeO_3$ films by UV–visible absorption and cathodoluminescence spectroscopies. *Appl. Phys. Lett.* **92**, 222901 (2008).
45. Takada, Y. & Masaki, M. Polarons in Jahn-Teller crystals: Intrinsic difference between e_g and t_{2g} electrons. *J. Supercond. Nov. Magn.* **20**, 629–633 (2007).

Acknowledgements

The work is supported by the Director, Office of Science, Office of Basic Energy Sciences, Materials Sciences Division of the US Department of Energy under contract No. DE-AC02-05CH11231. C.-H.Y. would like to acknowledge the Korea Research Foundation Grant funded by the Korean Government (MOEHRD). (KRF-2006-214-C00020) J.S. acknowledges support from the Alexander von Humboldt Foundation. Y.H.C. would like to acknowledge the support of the National Science Council, R.O.C., under Contract No NSC 97-3114-M-009-001. A portion of this research was carried out as a user project at Oak Ridge National Laboratory's Center for Nanophase Materials Sciences, sponsored by the Scientific User Facilities Division, BES, US DOE.

Additional information

Supplementary information accompanies this paper on www.nature.com/naturematerials. Reprints and permissions information is available online at http://npg.nature.com/reprintsandpermissions. Correspondence and requests for materials should be addressed to C.-H.Y.